GSICS
Global Space-based Inter-Calibration System

Quarterly

Newsletter Fall 2021 Issue

doi: 10.25923/akmr-zc10
Vol. 15 No 3, 2021
Editor: Manik Bali, ESSIC/UMD

CMA • CNES • ESA • EUMETSAT • IMD • ISRO • JAXA • JMA • KMA • NASA • NIST • NOAA • ROSCOSMOS . ROSHYDROMET • SITP • USGS • WMO

Examination of all-sky infrared radiance simulation of Hiwamari-8 for global data assimilation

By K. Okamoto, M. Hayashi (JMA), T. Hashino (KUT), M. Nakagawa (JMA), and A. Okuyama (JMA)

Infrared radiances from space are crucially important for numerical weather prediction (NWP). While NWP centers have mainly assimilated in clear-sky conditions, all-sky radiance (ASR) assimilation is expected to bring more positive impacts on analyses and forecasts because of greater coverage, cloud information and improved sampling. Effective assimilation requires understanding how well forecast models and radiative transfer models (RTMs) reproduce ASR as well as characteristics of ASR observations. This understanding in turn will help to verify the forecast models and RTMs.

This study examined the differences between observations and model simulations (observation-minus-background or O – B) and their causes. The findings were used for development of data assimilation processing such as quality control (QC) and bias correction (BC). This article demonstrates some results of this examination and development with focus on water vapor bands of Himawari-8. The details are described in Okamoto et al. (2021).

Examination of O-B

To simulate ASR, we used JMA's operational Global Spectral Model (GSM; JMA, 2019) and RTTOV version 12.2 (Saunders et al., 2018). The horizontal grid spacing of GSM is about 20 km and the number of vertical layers is 100 up to 0.01 hPa. Large-scale cloud condensates and cloud covers are parameterized following Smith (1990) with a top-hat-shaped probability distribution function. The cumulus convection scheme employs Arakawa and Schubert (1974). The ice to cloud condensate ratio is diagnosed as a linear function of temperature between -15°C and 0°C. RTTOV ver. 12.2 employs a scaling approximation for cloud multiple scattering calculation (Chou et al., 1999), and a stream method to account for the partial cloud effect (Matricardi, 2005). We chose a Baran scheme in the ice optical property parameterization option (Vidot et al., 2015). For observations, instead of individual pixels with 2-km resolution, we used an ASR product which is averaged over 16×16 pixels to better match the grid spacing of GSM and to follow the size of the operational clear-sky radiance (CSR) product. The ASR product contains cloud fraction, average and standard deviations (SD) of the brightness temperatures (BT), and a fraction of cloud type. The ASR product was experimentally created by the Meteorological Satellite Center of JMA.

Figures 1a and 1b show the monthly

doi: 10.25923/akmr-zc10

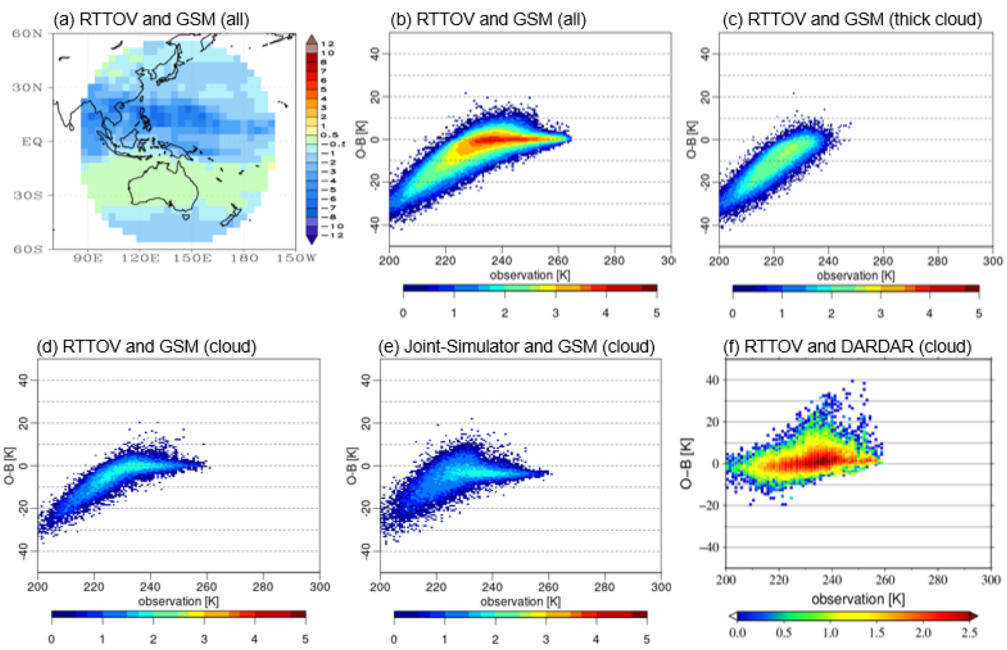

Figure 1. O – B statistics for band 8 of Himawari-8 in (a,b) all-sky, (c) thick cloud, (d,e) cloudy conditions. Background BT was calculated using (a-d, f) RTTOV version 12.2 and (e) Joint-Simulator with input ice cloud was given by (a-e) GSM and (f) DARDAR. (a) Monthly average O − B in 4° × 4° grid box. (b-f) Number of samples (on the log scale) as a function of O − B and observed BT. The samples were collected (a-e) from 1 to 31 August 2018 and (f) 16 to 31 August 2016.

averaged O – B and the number of samples of O – B and observed BT bins at band 8 (6.2 μm). Negative O – B values are evident where clouds are likely present and become larger for lower BT. BT less than 230 K at band 13 (10.4 μm) is not reproduced in the background (not shown). The negative bias is especially obvious for thick ice clouds (Fig. 1c). In contrast, there is a positive bias in relatively high BT region (Fig.1b). To investigate the cause of these biases, we choose cloudy samples with consistent cloud fraction between observation and background but the biases still existed (Fig. 1d). Thus, we examined other three possible bias sources

First, we examined the effect of RTM by using different RTMs that are believed to more accurately calculate cloud scattering and absorption. We used the Joint-Simulator (Hashino et al., 2013) that calculates the cloud multiple scattering for infrared BT using a discrete ordinate and adding method and employs optical properties on the basis of particle size distribution and mass–dimensional relationship for each hydrometeor category so that they are consistent with those defined in forecast models. The simulations using Joint-Simulator show similar distribution to those when using RTTOV despite slightly smaller negative O − B bias and SD (Fig.1e). This indicates that all the biases cannot be explained by the RTM.

Second, we validated the observation's calibration, especially at low BT, based on a GSICS framework. The calibration bias was estimated by using the difference from a reference made by spectrally integrated IASI observations. The linear regression of the difference at 220 K shows -0.18 K ± 0.04 K. These biases are much smaller than O − B biases, suggesting that the calibration bias cannot be main factor of the biases.

Finally, we compared O − B by using ice cloud input from GSM and more reliable dataset. Here we used ice cloud profiles from the raDAR/liDAR (DARDAR) project (Delanoë and Hogan, 2010) which was made by synergetic measurements of the CloudSat radar and the CALIPSO lidar. Simulations using DARDAR and RTTOV substantially removed the negative O − B bias (Fig. 1f), suggesting the negative bias was mainly caused by cloud underestimation of GSM. Because these samples were collected where cloud fractions of the observations and GSM were consistent, GSM could underestimate the cloud condensates too. In contrast, Figure 1f still shows the evident positive O − B bias at high observed BT, larger than those in the GSM simulation. This suggests excessive cloud absorption in the RTMs (both RTTOV and Joint-Simulator). Given that the extinction of thin ice clouds considerably varies with the cloud optical and microphysical parameters such as effective radius, more appropriate cloud optical and microphysical parameters may be necessary.

Application to data assimilation processing

We are developing data assimilation processing on the basis of the findings of O − B statistics and the bias sources described in the previous section. For example, the QC excluded samples that have observed BT at band 13 lower than 230 K and when thick ice clouds were dominant. Also, based on the previous study (Okamoto, 2017), we removed samples with large O – B, high inhomogeneity, and affected by aerosol, of which the latter two QC utilise ASR product information. Figure 2 shows results of the QC at bands 8 and 10 (7.3 μm): Samples at low observed BT and having negative O − B were expectedly removed and became more

doi: 10.25923/akmr-zc10

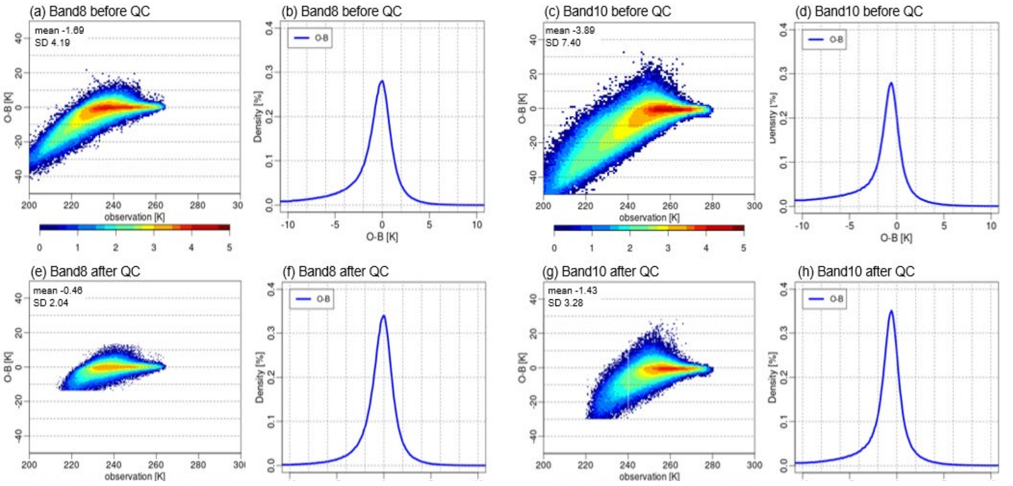

Figure 2. O – B statistics for bands 8 and 10 of Himawari-8 (a-d) before and (e-h) after QC in all-sky conditions. (a,c,e,g) Sample numbers as a function of O − B and observed BT with O – B mean and standard deviation plotted on the upper left of panel, and (b,d,f,h) Histograms of O – B.

symmetrical around O − B = 0. However, the negative bias remained at low BT region, especially at band 10, after the QC. We are now developing a bias correction that accounts for this negative bias dependent on cloud effect. Also, it is noticed that the peak is slightly shifted toward the negative side at band 10. Because this is similar to O-B in CSR (not shown), we are testing BC predictors by adding cloud effect parameters to CSR BC predictors with encouraging initial results.

4. Summary

To develop infrared ASR assimilation for Himawari-8, simulations from the global forecast model and radiative transfer model were carefully examined. The systematic differences between observations and simulations were caused by considerable deficit of high cloud in the forecast model and overestimated absorption of thin ice cloud in radiative transfer calculation. These results are used to develop QC and BC.

Cycle experiments show that impacts of Himawari-8 ASR assimilation are significantly positive but smaller than those of CSR assimilation. Thus, we need to further carefully investigate O − B statistics and enhance data assimilation processing. Also, we are planning to extend this work to infrared observations from other geostationary and low-earth orbiting satellites.

References

Arakawa, A. and Schubert, W. H. (1974). Interaction of a cumulus cloud ensemble with the large-scale environment, Part I. *Journal of the Atmospheric Sciences,* **31**, 674–701.
Chou, M. D., et al (1999). Parameterization for cloud longwave scattering for use in atmospheric models. *Journal of Climate*, **12**, 159–169.
Delanoë, J., and Hogan, R. J. (2010). Combined CloudSat-CALIPSO-MODIS retrievals of the properties of ice clouds. *Journal of Geophysical Research: Atmospheres*, **115**, D00H29, doi:10.1029/2009JD012346

Hashino, T., et al. (2013). Evaluating cloud microphysics from NICAM against CloudSat and CALIPSO. *Journal of Geophysical Research: Atmospheres*, **118**, 7273–7292. doi:10.1002/jgrd.50564

Japan Meteorological Agency (2019). Outline of the operational numerical weather prediction at the Japan Meteorological Agency. Available at http://www.jma.go.jp/jma/jma-eng/jma-center/nwp/outline2019-nwp/index.htm
Matricardi, M. (2005). The inclusion of aerosols and clouds in RTIASI, the ECMWF fast radiative transfer model for the infrared atmospheric sounding interferometer, *Technical Memorandum* **474**. ECMWF: Reading, UK.

Okamoto, K. (2017). Evaluation of IR radiance simulation for all-sky assimilation of Himawari-8/AHI in a mesoscale NWP system. *Quarterly Journal of the Royal Meteorological Society,* **143**, 1517–1527. doi:10.1002/qj.3022

Okamoto, K et al (2021). Examination of all-sky infrared radiance simulation of Himawari-8 for global data assimilation and model verification. *Quarterly Journal of the Royal Meteorological Society*, 1– 17. doi.org/10.1002/qj.4144

Saunders, R., et al. (2018). An update on the RTTOV fast radiative transfer model (currently at version 12). *Geoscientific Model Development Discussions*, **11**, 1–32. https://doi.org/10.5194/gmd-2018-64

Smith, R. N. B. (1990). A scheme for predicting layer clouds and their water content in a general circulation model. *Quarterly Journal of the Royal Meteorological Society,* **116**, 435–460.

Vidot, J., et al. (2015). A new ice cloud parameterization for infrared radiative transfer simulation of cloudy radiances: Evaluation and optimization with IIR observations and ice cloud profile retrieval products. *Journal of Geophysical Research: Atmospheres*, **120**, 6937–6951. doi: 10.1002/2015JD023462

doi: 10.25923/akmr-zc10

Rescuing Nimbus, DMSP and TIROS observations and preparing RTTOV for reanalysis

By J. Vidot (CNRM), E. Turner (Met-Office), B. Silveira (CNRM), P. Roquet (CNRM), P. Brunel (CNRM) and R. Saunders (Met-Office)

1. Introduction

A consortium led by SPASCIA with the University of Reading, CNRM, UK MetOffice and ICARE/AERIS is involved in the C3S 311c Lot1 “Satellite data rescue” project (2018-2021). The project aims to rescue, reformat, and standardize infrared and microwave satellites observations of the 1970s and 1980s to be used in the ECMWF ERA-6 reanalysis and potentially others. To assimilate these observations, one of the objectives is to prepare the satellite observation operator RTTOV (Saunders et al., 2018) to simulate these instruments based on the best knowledge about the instrument spectral response function (SRF) or pass-band filter. A second objective is to work on the observations minus background (O-B) statistics in order to (1) improve the knowledge about the instruments (SRF or pass-band filter) and (2) prepare the bias correction of these instruments.

2. Objectives for radiative transfer model

The first objective for the radiative transfer model was to provide the RTTOV clear-sky coefficients for all instruments listed in Table 1 and for different versions of RTTOV predictors, version 7 and 8 used up to now and the new RTTOV transmittance model, version 13 (Hocking et al., 2021). The second objective was to provide a global evaluation of the performance of RTTOV coefficients based on a large profile dataset. The third objective is to generate RTTOV coefficients for pseudo hyperspectral IR instruments (from 200 to 3000 cm^{-1}) with a boxcar SRF at 0.5 cm^{-1} width to study the impact of potential SRF shifts on the O-B values. The last objective was to provide forward model errors based on underlying spectroscopy variability or improved spectroscopy.

3. Global evaluation of clear-sky RTTOV simulation errors

The current validation of RTTOV coefficients is based on the comparison between clear-sky LBL simulations versus RTTOV on the 83 training profiles used for coefficient generation. The coefficient generation is based on two LBL models: LBLRTM (Clough et al., 2005) for IR and AMSUTRAN (Turner et al., 2019) for MW. A more complete validation was based on the independent 25000 diverse profiles dataset of the NWPSAF at 137 levels (Eresmaa and McNally, 2014). Figure 1 shows an example of the results of the map of the difference between RTTOV and LBLRTM for a SIRS channel centered at 899 cm^{-1}. The use of the NWPSAF 137 levels diverse profile dataset allows us to show the global distribution of the differences and the latitudinal effects of the RTTOV errors

Name	Platform	IR channels	V7	V8	V13
IRIS-D	Nimbus-4	400-1600 cm^{-}	No	Yes	Yes
MRIR	Nimbus-2 and 3	4	Yes	Yes	Yes
THIR	Nimbus-4 to 7	2	Yes	Yes	Yes
SIRS	Nimbus-3 and 4	7 (+6)	No	Yes	Yes
HRIR	NIimbus-1 to 3	1	No	Yes	Yes
		MW			
SMMR	Nimbus-7	10	Yes	No	Yes
SSM/T2	DMSP F11-F15	5	Yes	No	Yes
MSU	TIROS-N-	4	Yes	No	Yes
SSM/I	DMSP F8,F10-	7	Yes	No	Yes
SSMI(S)	DMSP F16-F19	24	Yes	No	Yes

Table 1. List of instruments studied in the C3S project

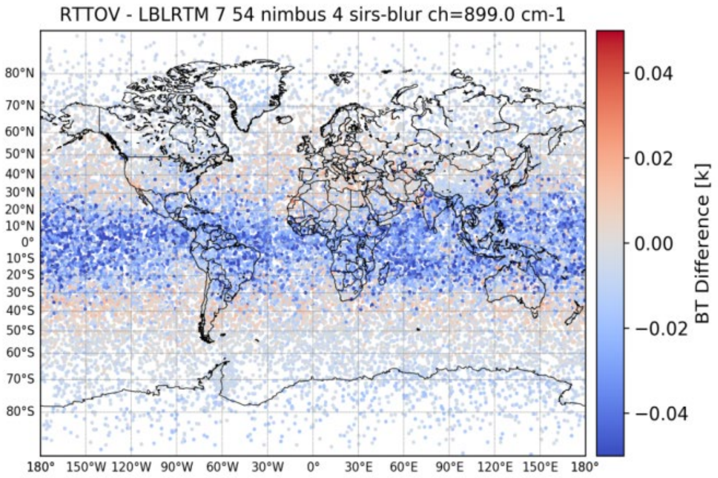

Figure 1. Map of RTTOV minus LBLRTM from the NWPSAF 137 levels diverse profile dataset for SIRS-B window channel at 899.cm^{-1}.

doi: 10.25923/akmr-zc10

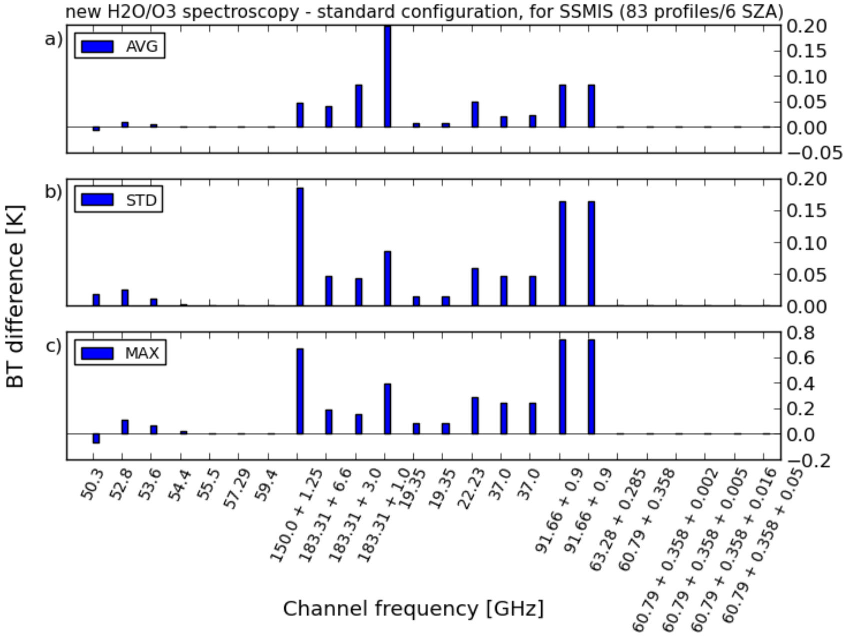

Figure 2. BT difference between original RTTOV and new MW spectroscopy for SSMIS.

compared with LBL with higher errors (up to 0.04 K) in tropical regions probably due to higher water vapour concentration.

4. Spectroscopy study

In clear-sky simulations, unknowns coming from the underlying spectroscopy are the main source of forward modelling errors. Figure 2 show the Brightness Temperature (BT) difference for SSMIS channels due to alternate RTTOV coefficients with new MW spectroscopy. In this new spectroscopy configuration, the water vapour and ozone were updated with AER version 3.6 line database and the MT-CKD 3.2 water vapour continuum model. The mean and standard deviation of the differences are below 0.2K using the RTTOV 83 profiles and for 6 secants (cosine of the viewing zenith angle), however, maximum values of 0.7 K are possible in window channels due to the different representations of the continuum.

In the project, we also compared the standard deviations of the BT difference from the use of three versions of LBLRTM (11.1, 12.2 and 12.8) with the IRIS and IASI noise (not shown). We found that the large noise of IRIS (in NeDT from 0.5 to 3 K at the edges of the band) makes the observations insensitive on average to the underlying spectroscopy (with maximum standard deviation of 0.3 K below 600 cm^{-1}), whereas IASI is sensitive in the water absorption band above 1200 cm^{-1}.

5. Conclusion

In this project we prepared the forward model RTTOV versions 12 and 13 to simulate early IR and MW satellite observations for the next ERA reanalysis. We evaluated the clear-sky RTTOV errors by comparing with LBL models and by using a large independent profile dataset. The evaluation showed for the first time a slight latitudinal effect of RTTOV errors that may be considered in bias correction methods. We showed that the error due to underlying spectroscopy is low compared with the noise of early satellites but is at the same level of accuracy of the current satellite measurements.

6. References

Saunders, R., Hocking, J., Turner, E., Rayer, P., Rundle, D., Brunel, P., Vidot, J., Roquet, P., Matricardi, M., Geer, A., Bormann, N., and Lupu, C.: An update on the RTTOV fast radiative transfer model (currently at version 12), Geosci. Model Dev., 11, 2717-2737, https://doi.org/10.5194/gmd-11-2717-2018, 2018.

Eresmaa R. and McNally A: Diverse profiles dataset from the ECMWF 137-level short-range forecasts, 2014. See: https://www.nwpsaf.eu/site/software/atmospheric-profile-data/

Hocking, J., Vidot, J., Brunel, P., Roquet, P., Silveira, B., Turner, E., and Lupu, C.: A new gas absorption optical depth parameterisation for RTTOV version 13, Geosci. Model Dev., 14, 2899–2915, https://doi.org/10.5194/gmd-14-2899-2021, 2021.

Turner,E., Rayer, P. and Saunders, R.: AMSUTRAN: A microwave transmittance code for satellite remote sensing, J. of Quantitative Spectroscopy and Radiative Transfer, 227,https://doi.org/10.1016/j.jqsrt.2019.02.013, 2019.

Clough S.A., Shephard M.W., Mlawer E.J., Delamere J.S., Iacono M.J., Cady-Pereira K., Boukabara S., Brown P.D.: Atmospheric radiative transfer modeling: a summary of the AER codes, Journal of Quantitative Spectroscopy and Radiative Transfer, Volume 91, Issue 2,https://doi.org/10.1016/j.jqsrt.2004.05.058, 2005.

doi: 10.25923/akmr-zc10

VIIRS Relative Spectral Response Effects on Solar Diffuser Degradation and On-Orbit Radiometric Calibration

By Taeyoung (Jason) Choi (GST/NOAA) and Changyong Cao (NOAA)

Introduction

For on-orbit imaging sensors, the Solar Diffuser (SD) became a standard radiometric calibration source for historical Moderate Resolution Imaging Spectroradiometer (MODIS), Landsat Operational Land Imager (OLI), and Visible Infrared Imaging Radiometer Suite (VIIRS) instruments. For VIIRS sensors, the Angle Of Incidence (AOI) was intentionally designed to have 60.4 degrees to the Half-Angle-Mirror (HAM) at the SD and Space View (SV) viewing angles. The purpose of having the same angle at SD and SV angles was to have the same viewing condition for the on-orbit SD and lunar calibrations. Even after having the same AOI angle between SD and lunar calibration (through SV port), there were long-term trend differences between the SD and lunar calibrations. To compensate for these differences, different agencies developed their own correction methodologies such as 'phenomenological model' by NASA, 'hybrid method from the nonuniform SD degradation' by the NOAA ocean color team, and 'Kalman filtering method' from the NOAA VIIRS Sensor Data Record (SDR) team [1, 2].

To simulate systematic long-term differences between the SD and lunar calibrations, a new SD degradation estimation algorithm is developed and applied using the relative spectral responses (RSR) of the Solar Diffuser Stability Monitor (SDSM) instead of using conventional center wavelength (CW)-based SD degradation interpolation.

VIIRS On-orbit Radiometric Calibration

Figure 1 shows simplified schematic of SD, SDSM and VIIRS Rotating Telescope Assembly (RTA) for on-orbit Reflective Solar Band (RSB) calibration. As a separate sensor, the SDSM monitors the SD degradations (called H-factors) by taking the ratio between the Sun and SD view responses denoted as digital counts (DC) with screen transmittance corrections.

$$H\ factor(t) \propto \frac{dc_{SD}(t)}{dc_{SUN}(t)} \qquad (1)$$

The primary on-orbit radiometric calibration coefficients (called F-factors) are calculated by the SD observations through RTA view as shown in Figure 1.

$$F\ factor(t) = \frac{RVS_{SD} \cos\left(\theta_{inc}(t)\right)\left\{E_{sun}\tau_{SDS}BRDF_{RTA}\frac{H(t)}{H(t_0)}\right\}}{SD\ observed\ radiance\ from\ RTA}$$
(2)

In Equation (2), RVS_{SD} is Response Versus Scan (RVS) at SD viewing angle, E_{sun} is the solar irradiance value which is modulated by the VIIRS detector RSR, the $\tau_{SDS}BRDF_{RTA}$ is the SD screen modulated Bidirectional Reflectance Distribution Fruition (BRDF) of the SD at

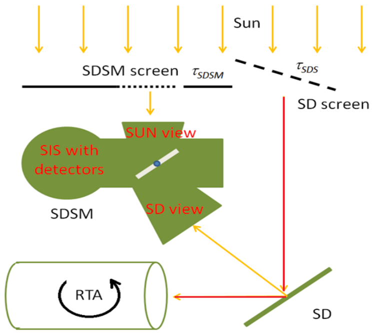

Figure 1. A simplified schematic of screens, SD, SDSM and RTA relations with illumination from the Sun.

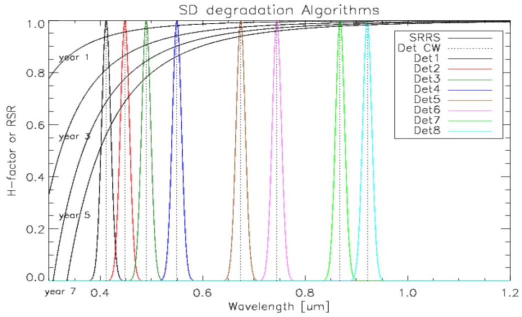

Figure 2. The SRRS simulation of the H-factor estimation algorithms for the CW method and the RSR weighted sum approach.

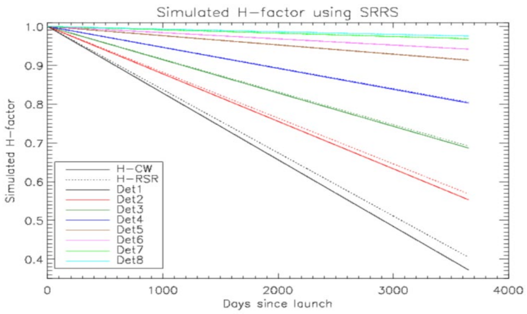

Figure 3. Time-dependent SRRS simulation result over 10 years of operation

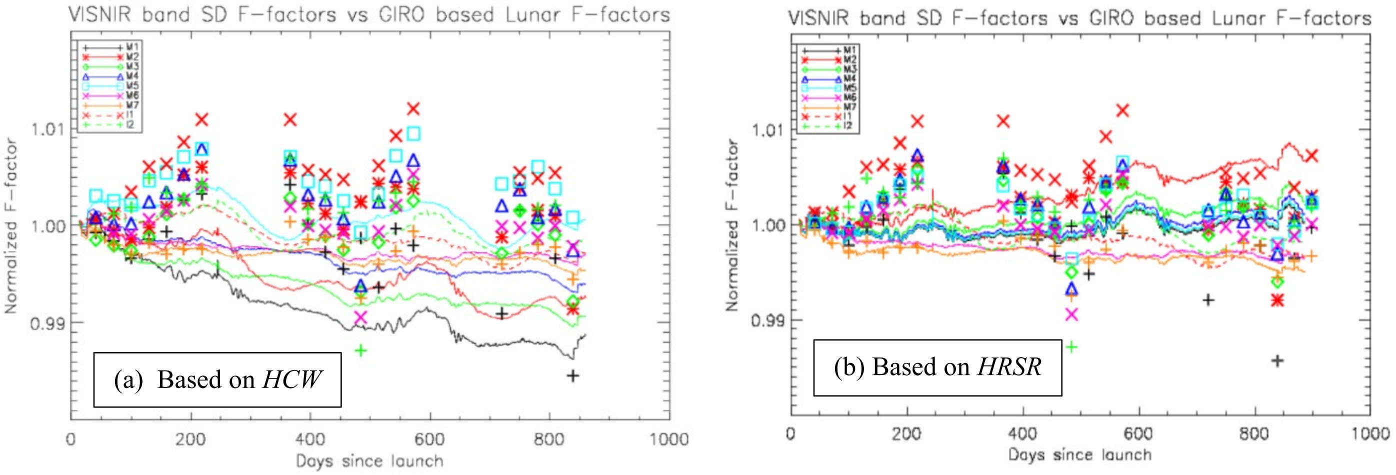

Figure 4. Long-term trend comparisons of the NOAA-20 VIIRS SD F-factors (lines) and lunar F-factors (symbols) with *HCW* and *HRSR*.

the RTA view angle, and $\frac{H(t)}{H(t_0)}$ is the normalized SD H-factor that linearly interpolated at the band-averaged VIIRS detectors. The H-factors of the VIIRS detector are linearly interpolated from the SDSM detector CWs to the VIIRS CWs.

Surface Roughness Rayleigh Scattering (SRRS) Simulation

The SRRS model has been developed and fitted to the NOAA-20 VIIRS case using its on-orbit H-factors with the roughness factor of 0.018 μm^2 per year and the fourth order over the wavelength as shown in Equation 3. All the H-factors from launch to 900 Days Since Launch (DSL) were used to derive the SRRS model. The SRRS simulation was performed to provide 10 years synthetic SD degradation with finely sampled time and wavelength domains. In Figure 2, black solid lines show the simulated SRRS model SD degradation after one, three, and 5 years. There were two types of H-factors. One is CW-based H-factors (*HCW*) and the other is RSR-based H-factors (*HRSR*). The *HCW* and *HRSR* are shown as dotted lines and colored Gaussian Functions in Figure 2, respectively. The SDSM RSRs are established with Gaussian functions for visualization purposes because the actual SDSM RSR data are not publicly available. But the further results were derived from the measured SDSM RSRs.

$$SRRS(t,\lambda) = 1 - \frac{0.018\, t[\mu m^2/year]}{\lambda^{4.0}} \quad (3)$$

Figure 3 shows the simulated *HCW* and *HRSR* results over ten years. Growing time-dependent differences are observed especially for the short wavelength detectors from 1 to 4. These increasing differences were caused by the different rates of change over the RSR ranges. In addition, the differences were very sensitive to the Out-Of-Band (OOB) response of the SDSM detector RSRs. When the SDSM detector RSRs were considered, all the *HRSR* responses were higher than the *HCW* results from the simulation except the SDSM detector 4. For SDSM detector 4, constant spectral leaks were found below 470nm on the left side of the main lobe, which caused lower *HRSR* than *HCW*. After removing the RSR response below 470nm, the direction of H-factor ratio returned to normal (positive) compared to other detectors. For other longer wavelength detectors, the differences were very small (mostly less than 0.25%) over ten years. These results indicated that the current CW-based H-factor overestimated the SD degradation especially in the short wavelength.

Applying *HRSR* to NOAA-20 VIIRS RSB Calibration

Besides the primary SD calibration, VIIRS can view the moon monthly (except summer months) and the lunar F-factors were derived as shown as symbols in Figure 4. The solid lines represent the SD F-factors in the figure. To validate the long-term trends of the primary SD F-factors, lunar F-factors were normalized to the 2nd lunar collection on January 27, 2018. Figure 4(a) shows SD F-factors with *HCW* whereas Figure 4(b) shows SD F-factors with *HRSR*. Even though lunar F-factors (symbols) show annual oscillations mostly within ±1% level, they didn't show significant sings of long-term trend changes. On the other hand, there are growing differences between the lunar and SD F-factors in the short wavelength bands of M1 to M4 in Figure 4(a) with the

doi: 10.25923/akmr-zc10

conventional *HCW* approach. After applying newly developed *HRSR*, SD F-factors became very consistent with lunar F-factors in Figure 4(b).

Conclusions

An RSR based SD degradation algorithm is developed, simulated and applied to NOAA-20 VIIRS RSB calibration. Using SRRS simulation, the CW based H-factors over-estimated SD degradation when they were compared to the detector RSR weighted H-factors. Short wavelength SDSM detectors 1 to 4 showed significant differences because of non-linear behavior of the SD degradation process. The SDSM detector 1 showed almost 1.5% difference around 800 days after launch. These simulation results were applied back to the on-orbit calibration coefficients (called F-factors) and the long-term trends of the SDF-factors were validated by the lunar F-factors. The corrected SD F-factors and lunar F-factors showed consistent RSB long-term trends over two years of RSB calibration. With the known large OOB responses in the JPSS-2 VIIRS SDSM RSRs, this algorithm can be applied to estimate actual SD degradation over the operational wavelength range, reducing the possible differences between SD and lunar radiometric calibrations.

References

[1] C. Cao *et al.*, "Mission-Long Recalibrated Science Quality Suomi NPP VIIRS Radiometric Dataset Using Advanced Algorithms for Time Series Studies," *Remote Sensing,* vol. 13, no. 6, p. 1075, 2021.

[2] T. Choi, X. Shao, and C. Cao, "On-orbit radiometric calibration of Suomi NPP VIIRS reflective solar bands using the Moon and solar diffuser," *Appl Opt,* vol. 57, no. 32, pp. 9533-9542, Nov 10 2018.

Uncertainty Estimates in Sentinel-3 SLSTR Level-1 Data

By David Smith, STFC RAL Space

The Sea and Land Surface Temperature Radiometer (SLSTR) on the Copernicus Sentinel-3 mission is an instrument designed to retrieve global sea surface temperatures (SSTs) for climate monitoring [Coppo et al. 2010]. Two satellites (models A and B) are currently on-orbit to provide near complete daily global coverage. SLSTR is a development of the along-track scanning radiometer (A)ATSR series and shares many of the key design features needed for accurate measurement of SST.

At the most basic level, the quality of the level-1 data is defined in terms of its uncertainty and traceability to standard references. For a Thermal InfraRed (TIR) instrument such as SLSTR, the radiometric calibration is performed using two on-board blackbody sources. The radiances from the blackbodies are derived via Planck's radiation law and traced to the temperatures which are measured by Platinum Resistance Thermometers (PRTs). These were calibrated on ground against Standard-PRTs which in turn were calibrated against standard artefacts such as a water triple point phase change cell to provide traceability to ITS-90. The actual situation is not so simple however, because the processing of the raw satellite data (Level-0 data) to radiometrically calibrated and geo-referenced data products (Level-1 data) involves several processing steps and relies on several input sources that in turn will be derived from models or measurements. Thus, the uncertainty of the data products is dependent on several effects contributing to the data processing.

To derive uncertainty estimates for the SLSTR Level-1 channels, Smith et al. (2021) have adopted the approach developed by the FIDUCEO project (FIDelity and Uncertainty in Climate data records from Earth Observation) [Mittaz et al. 2019], which was established to provide a metrological framework to address the need for improving the traceability and quantifying uncertainty estimates in EO datasets.

doi: 10.25923/akmr-zc10

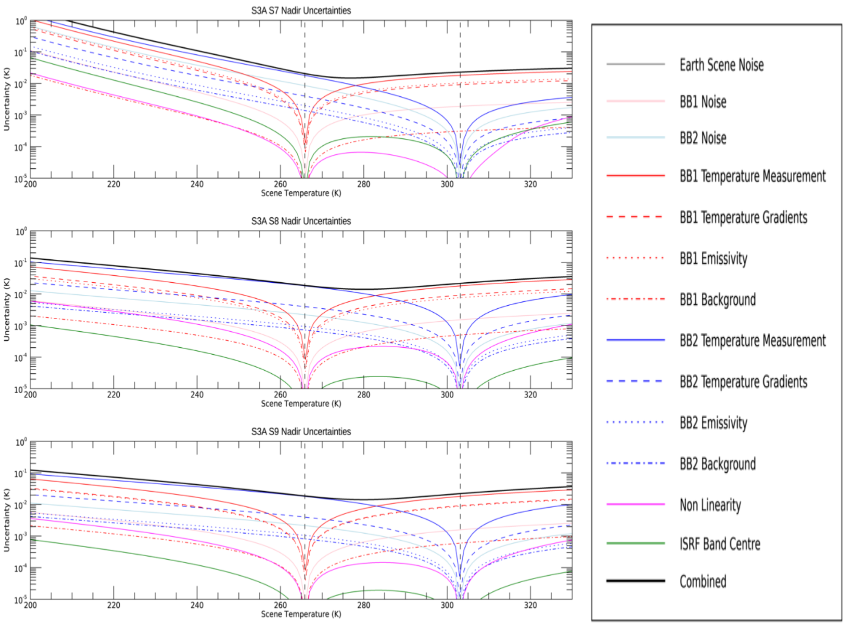

Figure 1. SLSTR-A Thermal Infrared Uncertainty Budget for a typical orbit at 1 June 2020.

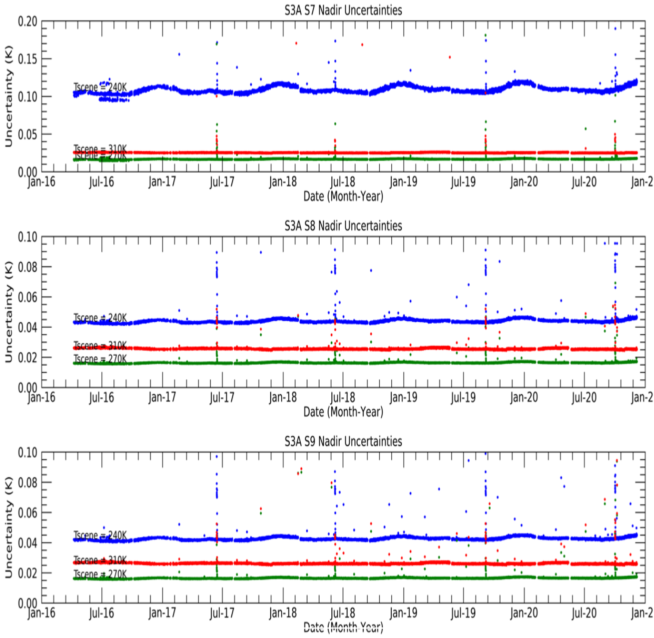

Figure 2. Time series for the period from March 2016 to December 2020 of SLSTR-A Thermal Infrared Radiometric. Uncertainties (systematic effects) for scene temperatures of 240 K (blue), 270 K (green) and 310 K (red).

The starting point is the mathematical description of the measurement function that establishes the mathematical relationship between all known input quantities (e.g. instrument counts) and the measurand itself (e.g. Brightness Temperature in K). Generally, this may be written as, $y = f(x_1, x_2 \dots x_n)$ where y is the measurand, and x_i are the input quantities. The uncertainty analysis is then performed by considering in turn each of these different input quantities to the measurement function, where each input quantity may in-turn be influenced by one or more error effects which are described by an uncertainty distribution. A useful approach for the uncertainty analysis is by using graphical representation of the sensor measurement function, called the uncertainty tree diagram. Starting with the measurement function, the contributing effects are identified which can either be directly traced to a simple measurement with an uncertainty estimate, or in turn are a function with other input effects. The effects tree is then continued out until the root effects are reached. Each of the effects identified at the end of each of the branches should then be understood, quantified, and reported in an “Effects Table” which documents, the uncertainty, sensitivity coefficients, distribution functions and the correlation structure for the given effect. Having documented the input effects, these are then combined to determine the uncertainty of the measurand, using the Law of Propagation of Uncertainties (GUM, 2008).

An example of the uncertainty budget in the radiometric calibration for SLSTR-A is shown in Figure 1 for 1 June 2020 where the instrument was in their nominal flight operational configuration. The budget shows that between the temperatures of the two on-board blackbody sources, the uncertainties are dominated by the blackbody temperature measurements and the baseplate gradients. Other effects are small by comparison. Outside the temperature range of the on-board blackbodies, effects such as non-linearity and spectral response begin to contribute but are still smaller than the contribution from the on-board BB temperatures. We can also use the uncertainty model to evaluate the effect of in-flight variations of the instrument behaviour. For example, the temperatures of the SLSTR instruments vary with season by ~2°C, being warmer in northern hemisphere winter months. Applying the model to instrument detector counts and temperatures extracted from the instrument’s Level-0 science data we can derive time series of the radiometric uncertainties as shown in Figure 2 for SLSTR-A.

The Level-1 products contain estimates of both “random uncertainties” (uncertainties associated with independent/random effects) and “correlated uncertainties” (uncertainties associated with common/correlated effects). Ideally these uncertainty components would be provided per pixel and per channel, but that was unpractical at the time of the mission development when the processing chains and product specifications were being defined. Instead, we have developed a tool, ‘MapnoiS3’ to map the random and correlated uncertainties to the Level-1 image grid. The tool allows the level-1 uncertainty estimates to be propagated further to level-2 and higher-level products.

Evaluating uncertainties in the Level-1 data is an on-going process, and the estimates reported are those accounted for in the data processing chain. The uncertainty budget will be revised as additional effects are assessed, such as internal stray light. For future missions, establishing the uncertainty budget and document the traceability chain should be part of the routine design and development phase of the mission to ensure the scientific readiness of the data.

This work was funded European Union’s Copernicus Programme, and managed by the Europe-an Organization for the Exploitation of Meteorological Satellites through the contract EUM/CO/18/4600002122/AOC. It has also received funding from the project MetEOC-3 (16ENV03) of the EMPIR programme co-financed by the Participating States and from the European Union’s Horizon 2020 research and innovation programme.

References:

Coppo, P.; Ricciarelli, B.; Brandani, F.; Delderfield, J.; Ferlet, M.; Mutlow, C.; Munro, G.; Nightingale, T.; Smith, D.; Bianchi, S.; et al. SLSTR: A high accuracy dual scan temperature radiometer for sea and land surface monitoring from space. J. Mod. Opt. **2010**, 57, 1815–1830. https://doi.org/10.1080/09500340.2010.503010

Mittaz, J.; Merchant, C.J.; Woolliams, E.R. Applying principles of metrology to historical Earth observations from satellites. Metrologia **2019**, 56, 032002, https://doi.org/10.1088/1681-7575/ab1705

Smith, D.; Hunt, S.E.; Etxaluze, M.; Peters, D.; Nightingale, T.; Mittaz, J.; Woolliams, E.R.; Polehampton, E. Traceability of the Sentinel-3 SLSTR Level-1 Infrared Radiometric Processing. *Remote Sens.* **2021**, *13*, 374. https://doi.org/10.3390/rs13030374

NEWS IN THIS QUARTER

Landsat-9 launched on September 27, 2021, beams down initial images

By Manik Bali (ESSIC/NOAA)

On September 27, 2021, Landsat 9 was launched from Vandenberg Air Force Base, California, onboard a United Launch Alliance Atlas V 401 rocket.

Landsat-9 will replace Lansat-7, it path offset from the Landsat-8 orbital track by eight days, and will provide continuity to the series of Landsat missions that began in 1972. The mission vision is to advance the scientific study of land change and land use into the next half-century at a scale where we can separate human and natural causes of change. To accomplish this goal Landsat-9 carries two science instruments. These are (Operational Land Imager) OLI-2 and (Thermal Infrared Sensor) TIRS-2. Radiometrically, these instruments are better version of similar instruments onboard the earlier Landsat platforms. Both instruments have sensors with moderate spatial resolution – 15 m, 30 m and 100 m depending on the spectral band – and the ability to detect a higher range of intensities than Landsat 8 (14-bit radiometric resolution vs. Landsat 8's 12-bit radiometric resolution). Landsat 9 will be placed in an orbit that it is eight days out of phase with Landsat 8 to increase temporal coverage of observations providing nearly 1,500 new scenes a day that will be archived in the USGS Landsat archive.

Landsat as an inter-calibration platform

From a GSICS standpoint, Landsat-9 will play a crucial role in the future inter-calibration activities. Landsat-9 has a superior design for radiometric accuracy than previous Landsat-9 spectrum and its channels overlap with most of the concurrently flying instruments that make observations in VIS/NIR wavelengths. For example, Landsat-9 and Sentinel-2 A/B cross the Equator within 1 hr in the morning / evening orbit ensuring similar solar illumination of targets observed and provide satellite inter-calibration comparison opportunities.

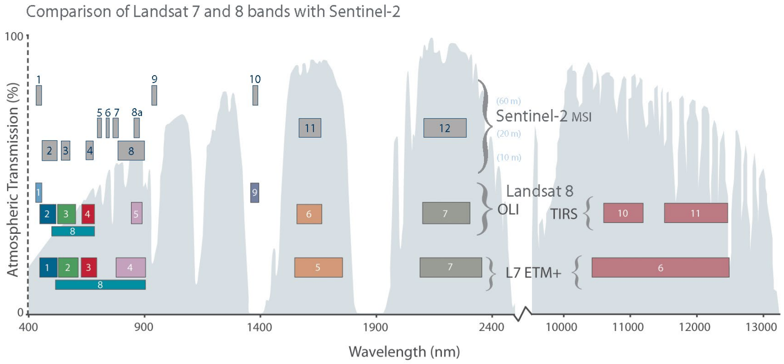

Figure Above(curtsey [USGS](#)) shows radiometric characteristics: The Landsat 8/9 have spectral bands very similar to Sentinel-2 A/B (excluding the thermal bands of Landsat 8/9's Thermal Infrared Sensor) thereby providing opportunity for intercalibration and product harmonization .

Landsat Data Sets and Tools

Landsat-9 datasets will be available from early 2022. Details about data availability of the Landsat series of satellites, and tools that can help analyse data can be found on the USGS website

https://www.usgs.gov/core-science-systems/nli/landsat/landsat-9?qt-science_support_page_related_con=0#qt-science_support_page_related_con

Announcements

SPIE Optics and Photonics Earth Observing Systems XXVII conference to be held in San Diego Aug 21-25, 2022

SPIE. The international society for optics and photonics

By Jack Xiong and James J. Butler (NASA) The annual SPIE Optics and Photonics' Earth Observing Systems XXVI Conference will be held August 21-25, 2022 at the San Diego Convention Center, San Diego, CA.

The Earth Observing Systems XXVII conference welcomes the submission of papers over a wide range of remote sensing topics. Papers are solicited in the following general areas:

- Earth-observing mission studies including new system requirements and plans
- commercial system designs
- electro-optical sensor designs and sensitivity studies
- ultraviolet through thermal infrared, microwave, radar, and lidar remote sensing systems
- hyperspectral remote sensing instruments and methodologies
- instrument sub-system and system level pre-launch and on-orbit calibration and characterization
- vicarious calibration techniques and results
- satellite instrument airborne simulators
- techniques for enhancing data processing, reprocessing, archival, dissemination, and utilization
- conversion from research to operational systems
- on-orbit instrument inter-comparison techniques and results
- enabling technologies (optics, antennas, electronics, calibration techniques, detectors, and models)
- sensor calibration traceability, uncertainty, and pre-launch to on-orbit performance assessments
- lunar radiometry and photometry
- re mote sensing data acquisition and analysis.

doi: 10.25923/akmr-zc10

The conference call for papers is available online at https://spie.org/OP22O/conferencedetails/earth-observing-systems Conference abstracts are due February 9, 2022, and proceedings manuscripts are due July 27, 2022.

GSICS-Related Publications

Bassani, C.; Sterckx, S. Calibration of Satellite Low Radiance by AERONET-OC Products and 6SV Model. *Remote Sens.* **2021**, *13*, 781. https://doi.org/10.3390/rs13040781

Chen, H.; Sun, C.; Xiong, X.; Sarid, G.; Sun, J. SNPP VIIRS Day Night Band: Ten Years of On-Orbit Calibration and Performance. *Remote Sens.* **2021**, *13*, 4179. https://doi.org/10.3390/rs13204179

Khakurel, P.; Leigh, L.; Kaewmanee, M.; Pinto, C.T. Extended Pseudo Invariant Calibration Site-Based Trend-to-Trend Cross-Calibration of Optical Satellite Sensors. *Remote Sens.* **2021**, *13*, 1545. https://doi.org/10.3390/rs13081545

Kim, K.; Lee, K. An Implementation of Open Source-Based Software as a Service (SaaS) to Produce TOA and TOC Reflectance of High-Resolution KOMPSAT-3/3A Satellite Image. *Remote Sens.* **2021**, *13*, 4550. https://doi.org/10.3390/rs13224550

Niro, F., P. Goryl, S. Dransfeld, V. Boccia, F. Gascon, J. Adams, B. Themann, S. Scifoni, and G. Doxani. 2021. 'European Space Agency (Esa) Calibration/Validation Strategy for Optical Land-Imaging Satellites and Pathway towards Interoperability'. *Remote Sensing* 13 (15). https://doi.org/10.3390/rs13153003.

Okamoto, K et al (2021). Examination of all-sky infrared radiance simulation of Himawari-8 for global data assimilation and model verification. *Quarterly Journal of the Royal Meteorological Society*, 1– 17. http://www.doi.org/10.1002/qj.4144

Song, P., and Y. Zhang. 2021. 'An Improved Non-Linear Inter-Calibration Method on Different Radiometers for Enhancing Coverage of Daily LST Estimates in Low Latitudes'. *Remote Sensing of Environment* 264. https://doi.org/10.1016/j.rse.2021.112626.

Staebell, C., Sun, K., Samra, J., Franklin, J., Chan Miller, C., Liu, X., Conway, E., Chance, K., Milligan, S., and Wofsy, S.: Spectral calibration of the MethaneAIR instrument, Atmos. Meas. Tech., 14, 3737–3753, https://doi.org/10.5194/amt-14-3737-2021, 2021.

Su, X., and G. Jiang. 2021. 'Intercalibration of FY-3D MWTS Against S-NPP ATMS Based on Microwave Radiative Transfer Model'. *IEEE Journal of Selected Topics in Applied Earth Observations and Remote Sensing*. https://doi.org/10.1109/JSTARS.2021.3104829.

Taylor, H.; Vreugdenburg, M.; Sangalli, L.; Vincent, R. RMCSat: An F10.7 Solar Flux Index CubeSat Mission. *Remote Sens.* **2021**, *13*, 4754. https://doi.org/10.3390/rs13234754

Weiler, F., Kanitz, T., Wernham, D., Rennie, M., Huber, D., Schillinger, M., Saint-Pe, O., Bell, R., Parrinello, T., and Reitebuch, O.: Characterization of dark current signal measurements of the ACCDs used on board the Aeolus satellite, Atmos. Meas. Tech., 14, 5153–5177, https://doi.org/10.5194/amt-14-5153-2021, 2021.

Xia, X., and X. Zou. 2021. 'Combining FY-3D MWTS-2 with AMSU-A Data for Inter-Decadal Diurnal Correction and Climate Trends of Atmospheric Temperature'. *Remote Sensing* 13 (16). https://doi.org/10.3390/rs13163148.

doi: 10.25923/akmr-zc10

Submitting Articles to the GSICS Quarterly Newsletter:

The GSICS Quarterly Press Crew is looking for short articles (800 to 900 words with one or two key, simple illustrations), especially related to calibration / validation capabilities and how they have been used to positively impact weather and climate products. Unsolicited articles may be submitted for consideration anytime, and if accepted, will be published in the next available newsletter issue after approval / editing. Please send articles to manik.bali@noaa.gov.

With Help from our friends:

The GSICS Quarterly Editor would like to thank Tim Hewison (EUMETSAT), Sri Harsha Madhavan (SSAI), Cheng-Zhi Zou (NOAA), Tom Stone (USGS) and Lawrence Flynn (NOAA) for reviewing articles in this issue. Thanks are due to Jan Thomas (NOAA) for helping with 508 compliance.

Published By

GSICS Coordination Center
NOAA/NESDIS/STAR NOAA
Center for Weather and Climate Prediction,
5830 University Research Court
College Park, MD 20740, USA

CISESS
5825 University Research Court, Suite 4001,
University of Maryland, College Park, MD 20740-3823